Atmospheric
Measurement
Techniques
Open Access
Discussions

Differential absorption radar techniques – Part 1: Surface pressure

L. Millán[1,2], M. Lebsock[2], N. Livesey[2], S. Tanelli[2], and G. Stephens[2]

[1]Joint Institute for Regional Earth System Science and Engineering, University of California, Los Angeles, California, USA
[2]Jet Propulsion Laboratory, California Institute of Technology, Pasadena, California, USA

Correspondence to: L. Millán (luis.f.millan@jpl.nasa.gov)

Discussion Paper | Discussion Paper | Discussion Paper | Discussion Paper

AMTD

7, 5795–5827, 2014

DiAR surface pressure retrievals

L. Millán et al.

Title Page

Abstract	Introduction
Conclusions	References
Tables	Figures

◀◀　　▶▶

◀　　▶

Back　　Close

Full Screen / Esc

Printer-friendly Version

Interactive Discussion

Abstract

Two radar pulses sent at different frequencies near the 60 GHz O_2 absorption band can be used to determine surface pressure by measuring the differential absorption on and off the band. Results of inverting synthetic data assuming an airborne radar are presented. The analysis includes the effects of temperature, water vapor, hydrometeors as well as particle size distributions and surface backscatter uncertainties. Results show that an airborne radar (with sensitivity of -20 and 0.05 dBZ speckle and relative calibration uncertainties and a 400 m by 400 m footprint) can estimate surface pressure with a precision of ~ 1.0 hPa and accuracy better than 1.0 hPa for clear-sky and cloudy conditions and better than 3.5 hPa for precipitating conditions. Generally, accuracy would be around 0.5 and 2 hPa for non-precipitating and precipitating conditions, respectively.

1 Introduction

Surface pressure is an essential variable in atmospheric dynamics and numerical weather forecasting. Historically, its spatial distribution has been used to reveal weather system patterns such as depressions, anticyclones, troughs, ridges and blocks. However, despite its importance, it is not yet available from remote sensing measurements and hence, there are large gaps in the measured surface pressure coverage, particularly over oceans.

Over the last decades, several techniques to remotely measure surface pressure have been proposed. All of them based upon comparing radiation backscatter in an O_2 band with the radiation in a nearby atmospheric window. In other words, one measurement needs to be sufficiently far into the band (on line) to be notably affected by changes in the O_2 total mass while the other needs to be on the wing of the band (off line) and in consequence barely affected by O_2 absorption. The ratio of these

measurements, or the differential absorption, is then a measure of the O_2 column abundance and since O_2 is a well mixed gas, a proxy for surface pressure.

The basic idea was proposed by Hanel (1961) for the estimation of cloud top height from a satellite. The method was based on measuring the absorption of cloud-reflected sunlight in the 2 µm CO_2 band. Yamamoto and Wark (1961) improved these method by recommending the 0.76 µm O_2 A-band instead, region with stronger signal and minimal interference from other species. Promptly, several authors (Singer, 1968; Smith et al., 1972; Barton and Le Marshall, 1979; Korb and Weng, 1982) proposed to use the same band but with a laser as a light source instead of the Sun. This technique is known as Differential Absorption Lidar (DiAL). Barton and Scott (1986) suggested a passive instrument following Yamamoto and Wark (1961) but focusing on the surface as a reflecting layer. However, due to the inability of visible radiation to penetrate clouds, these pressure measurements are restricted to clear sky areas and above clouds elsewhere. Furthermore, the passive instrument is restricted to daytime measurements only.

Flower and Peckham (1978) proposed the use of a Differential Absorption Radar (DiAR) in the 60 GHz (5 mm) O_2 band noting that at microwave frequencies the cloudy coverage limitation is greatly reduced. They investigated the use of up to six radar tones covering frequencies from $\sim$ 25 to $\sim$ 75 GHz. Such wide spectral region was needed to estimate the total water vapor column as well as the dry surface pressure. Recently, Lin and Hu (2005) and Lawrence et al. (2011) investigated a radar system with only two tones between 50 and 55 GHz. In this paper we revisit the DiAR concept. In Sect. 2, the physics of the radar echoes is discussed. Section 3 introduces a general model for computing radar echoes for any scene type (clear sky, cloudy or precipitating). Simulated differential absorptions measurements are cover in Sect. 4 and results of synthetic retrievals are discussed in Sect. 5. Results show that this technique has the potential of achieving $\sim$ 0.5 to 3.5 hPa (the latter for precipitating scenes) accuracy with realistically attainable airborne radar technology.

Title Page

Abstract | Introduction

Conclusions | References

Tables | Figures

|◄ | ►|

◄ | ►

Back | Close

Full Screen / Esc

Printer-friendly Version

Interactive Discussion

2 Theory

The return power measured by a monostatic radar which transmits a power P_T at wavelength λ can be simplified as,

$$P_R(\lambda, s) = \frac{P_T(\lambda) G^2 \lambda^2 \Omega}{(4\pi)^2 r^2} Y^2(\lambda, s) \eta(\lambda, s) \Delta r \tag{1}$$

where G is the antenna gain, r is the range to the target, Ω is the two-way solid angle, Δr is the range resolution, $\eta(\lambda, s)$ represents the hydrometeors as well as the surface ($\sigma^0(\lambda)$) backscatter coefficients, and $Y^2(\lambda, s)$ is the two-way transmission along the slant path s given by,

$$Y^2(\lambda, s) = \exp\left(-2\int_0^r \left[\sigma_{gas}(\lambda, s) + \sigma_{Pext}(\lambda, s)\right] ds\right) \tag{2}$$

where $\sigma_{gas}(\lambda, s)$ represents the gaseous absorption coefficient and $\sigma_{Pext}(\lambda, s)$ the particulate extinction (the sum of absorption and scattering) coefficient.

Equation (1) can be further simplified as,

$$P_R(\lambda, s) = \frac{C(\lambda) Y^2(\lambda, s) \eta(\lambda, s)}{r^2} \Delta r \tag{3}$$

where $C(\lambda) = P_T(\lambda) G^2 \lambda^2 \Omega / (4\pi)^2$ is the radar system parameter varying with the radar wavelength.

Assuming that the radar tones are chosen close to a strong absorption line, the wavelength dependence of $\sigma_{Pext}(\lambda, s)$ and $\eta(\lambda, s)$ is small relative to that of $\sigma_{gas}(\lambda, s)$ (see Fig. 1), the ratio of the return radar powers is given by,

$$\frac{P_R(\lambda_1, s)}{P_R(\lambda_2, s)} = \frac{C(\lambda_1)}{C(\lambda_2)} \frac{Y^2(\lambda_1, s)}{Y^2(\lambda_2, s)} \tag{4}$$

DiAR surface pressure retrievals

L. Millán et al.

Title Page

Abstract	Introduction
Conclusions	References
Tables	Figures

◄◄ ►►

◄ ►

Back Close

Full Screen / Esc

Printer-friendly Version

Interactive Discussion

where

$$\frac{Y^2(\lambda_1, s)}{Y^2(\lambda_2, s)} = \exp\left(-2\int_0^r \left[\sigma_{\text{gas}}(\lambda_1, s) - \sigma_{\text{gas}}(\lambda_2, s)\right] \mathrm{d}s\right) \tag{5}$$

which becomes,

$$\frac{Y^2(\lambda_1, s)}{Y^2(\lambda_2, s)} = \exp\left(-2\int_0^r \rho(s) \sum_i v_i(s)\left[\kappa_i(\lambda_1, s) - \kappa_i(\lambda_2, s)\right] \mathrm{d}s\right) \tag{6}$$

where $\rho(s)$ is the air density and the sum is over all the absorbers with monochromatic absorption coefficient $\kappa_i(\lambda, s)$ and volume mixing ratio $v_i(s)$.

Using the ideal gas law,

$$\frac{P_R(\lambda_1, s)}{P_R(\lambda_2, s)} = \frac{C(\lambda_1)}{C(\lambda_2)} \exp\left(-2\int_0^r \frac{p(s)}{RT(s)} \sum_i v_i(s)\left[\kappa_i(\lambda_1, s) - \kappa_i(\lambda_2, s)\right] \mathrm{d}s\right) \tag{7}$$

where R is the gas constant, p is pressure and T is temperature.

Furthermore, close to a strong absorption line, the monochromatic absorption coefficient for the rest of the absorbers (at two close enough wavelengths) are similar, leaving mostly the influence of the main absorber. For example, next to the 60 GHz O_2 absorption band, Eq. (7) can be simplified as,

$$\frac{P_R(\lambda_1, s)}{P_R(\lambda_2, s)} = \frac{C(\lambda_1)}{C(\lambda_2)} \exp\left(-2\int_0^r \frac{p(s)}{RT(s)} v_{O_2}(s)[\kappa_{O_2}(\lambda_1, s) - \kappa_{O_2}(\lambda_2, s)]\mathrm{d}s\right) \tag{8}$$

where, since the O_2 mixing ratio is well known, the only unknowns remaining are pressure and temperature. Then, it follows that assuming a temperature profile (e.g. from

analysis fields) it should be possible to retrieve surface pressure from the backscattered return from the Earth's surface.

In this study a pulsed radar system will be simulated to explore the expected uncertainty characteristics of surface pressure retrievals based on the physics of Eq. (7). We consider a radar minimum detectable signal (sensitivity) of −20 dBZ, speckle and relative calibration uncertainties of 0.05 dBZ, with a vertical resolution of 500 m and a horizontal resolution of 400 m by 400 m. These system parameters should be achievable from an airborne platform. We consider both instrument uncertainties and those associated with the assumptions necessary in the measurement inversion process.

3 Radar forward model

Simulated radar reflectivities were calculated computing the scattering properties of cloud and precipitation hydrometeors by means of Mie scattering theory, evaluating the gaseous absorption using the absorption coefficient calculations of the Clear-Sky Forward Model for the EOS Microwave Limb Sounder (MLS) (Read et al., 2006), estimating the single and multiple scattering by the hydrometeors using the fast time-dependent two-stream approximation described by Hogan and Battaglia (2008), and computing the ocean radar backscatter by a quasi-specular scattering model (Valenzuela, 1978; Brown, 1990; Li et al., 2005).

3.1 Optical constants

The dielectric properties of water and ice hydrometeors were taken from the parametrizations described by Liebe et al. (1991) and Hufford (1991), respectively. These parametrizations were developed using empirical fits to published experimental data and can be considered as an evolution of the commonly use Ray model (Ray, 1972).

3.2 Hydrometeors size distributions

3.2.1 Ice water content

We assume that all ice clouds can be described in terms of the McFarquhar and Heymsfield (1997) particle size distribution (PSD) parametrization derived from measurements during the Central Equatorial Pacific Experiment Campaign. This PSD characterizes the average properties of tropical ice crystal size distributions, dependent on temperature and IWC. This PSD is commonly used in cloud retrieval algorithms including that of the EOS-Microwave Limb Sounder (MLS), ODIN Sub-mm Radiometer, and the Superconducting Submillimeter-Wave Limb-Emission Sounder (SMILES) (Wu, 2006; Eriksson et al., 2007; Millán et al., 2013).

3.2.2 Liquid water content

Measurements using a wide variety of techniques show that the mean liquid cloud drop radius varies from 2 to around 16 μm depending on the type of cloud (Howell, 1949; Squires et al., 1958; Fitzgerald and Spyers-Duran, 1973; Tsay and Jayaweera, 1984; King, 1993; Gerber, 1996; Yum, 2002). In this study, we model liquid clouds using a lognormal distribution with a 10 μm median radius and a 1.3 spread. The lognormal distribution is described by,

$$n(r) = \frac{N_0}{\sqrt{2\pi}} \frac{1}{\log(\zeta)} \frac{1}{r} \exp\left(\frac{-(\log(r) - \log(r_m))^2}{2\log^2(\zeta)}\right) \tag{9}$$

where $n(r)$ is the number density of particles as a function of the radius r, N_0 is the total number of particles, r_m is the median particle radius of the size distribution, and where ζ is the spread of the distribution where the standard deviation of $\log(r)$ is equal to $\log(\zeta)$.

3.2.3 Rain

Precipitating liquid was distributed according to the Abel and Boutle (2012) PSD. This distribution was derived from in situ aircraft measurements in a wide variety of precipitation from stratocumulus to heavy stratiform rain. This PSD is described by an exponential function with variable intercept and slope parameters which are functions of the rain water content.

3.2.4 Snow

Precipitating ice was modeled using the snow size distribution of Sekhon and Srivastava (1970). An exponential function derived from extensive field studies.

3.3 Gas absorption

The absorption coefficient with respect to volume mixing ratio, κ^i for the ith species, was computed using,

$$\kappa^i = \kappa^i_{\text{LBL}} + \kappa^i_{\text{cont}} \tag{10}$$

where κ^i_{LBL} is the Line-By-Line cross section contribution described in Read et al. (2004, chap. 11) and Read et al. (2006) using a Voigt lineshape with a Van Vleck–Huber prefactor (Huber and Vleck, 1966; Buehler et al., 2005) and where κ^i_{cont} is the continuum contribution described in Read et al. (2004, chap. 12). Molecular line strengths and frequencies were taken from the HITRAN database (Rothman et al., 1998) and the JPL Spectroscopy Catalog (Pickett et al., 1998) in the same manner as the EOS MLS Molecular Line Catalog (Read et al., 2006).

3.4 TDTS approximation

Using the scattering properties and the gaseous absorption previously computed, we use the publicly available code described by Hogan (2013), which follows the

time-dependent two-stream (TDTS) approximation by Hogan and Battaglia (2008) to compute the time-dependent radar return. This model splits the photons in two categories, those that have only being affected by single scattering and those that have experienced wide-angle multiple scattering events. The time-dependent two-stream model has been shown to perform well in comparison with benchmark Monte Carlo Simulations in most clouds scenarios of interest here (i.e. not deep convection) while being more computationally efficient (Battaglia et al., 2010).

3.5 Ocean radar backscatter

Ocean surface backscattering properties were computed with the quasi-specular scattering model for low incidence angles described by Valenzuela (1978); Brown (1990) and Li et al. (2005). This model has been used in the external calibration of CloudSat (Tanelli et al., 2008) and the Radar Aéroporté et Sol de Télédétection des Propriétés Nuageuses (RASTA) (Bouniol et al., 2008). Mean-square surface slopes were taken from the empirical relationship described by Wu (1990), using the microwave dielectric constants for sea water modeled by Klein and Swift (1977). The incidence angle was assumed to be zero (nadir), the sea surface temperature 28 °C, wind surface was $3\,m\,s^{-1}$ and the Fresnel reflection coefficient correction factor 1 and zero salinity (which does not impact radar observables at around 60 GHz.

3.6 Forward model evaluation

A prerequisite for any synthetic retrievals discussion is a forward model evaluation. For this purpose, we use retrievals from CloudSat (Stephens et al., 2002) R04 algorithms as input to the forward model. The intent here is merely to demonstrate that our microphysical and radiative transfer models are consistent with those of the independent CloudSat retrieval algorithms. Here we use the 2B-GeoProf measurements, as well as, the LWC and IWC profiles from the 2B-CWC-RO R04, the rain and snow profiles from the 2C-RAIN-PROFILE retrieval products, and the temperature, pressure, water vapor

and ozone from the European Centre for Medium-Range Weather Forecasts auxiliary (ECMWF-aux) products. Description of the 2B-GeoProf measurements, the 2B-CWC-RO R04 and 2C-RAIN-PROFILE retrievals can be found in Marchand et al. (2008); Austin et al. (2009) and Lebsock and L'Ecuyer (2011), respectively. The ECMWF-aux data are ECMWF model outputs interpolated in time and space to the CloudSat measurements (Partain, 2007). Furthermore, we also use the 2B-CLDCLASS product (Sassen and Wang, 2008) for cloud classification.

For each validation scenario, the hydrometeors (IWC, LWC, rain, and snow) retrieved by CloudSat as well as the interpolated ECMWF model outputs (temperature, pressure, water vapor and ozone) were used as forward model inputs. Then, the forward model results were compared with the corresponding CloudSat returns that were used to retrieved such hydrometeors in the first place. Figure 2 shows a comparison between the forward model run and CloudSat measurements under two scenarios, a cirrus and a precipitating case (rain rate > 1 mm h^{-1}). In both cases, the forward model matches the CloudSat return, suggesting that the forward model assumptions are similar to the assumptions made in the CloudSat forward models used in such retrievals. Around 300 scenarios were simulated with an root mean square error (rms$_e$) of $\sim$ 3.5 dB.

4 Forward model simulations

Figure 3 shows clear sky simulated differential radar surface returns between 52.8 ($\sim$ 40 dBZ returns) and 54.9 ($\sim \pm 1$ dBZ returns) GHz and surface pressure under three thermal and three water vapor conditions. These radar tones are used because they were selected by Lin and Hu (2005) as the best combination among a subset of 6 tones. As shown, there is a linear relationship between the differential radar surface returns and surface pressure. The slope of this curve is the exploitable signal, which is on the order of 1 dB/20 hPa. This Figure shows that this signal is essentially insensitive to atmospheric water vapor burden but demonstrates a large sensitivity to the atmospheric temperature, which affects the pressure broadening of the lines within the

oxygen band. In particular, it is the temperature close to the surface that influences the signal the most.

To investigate the effect of clouds and rain, as in Sect. 3.6, we use CloudSat-driven simulations (i.e. using IWC, LWC, rain, snow, temperature, pressure, water vapor and ozone from CloudSat products) using data from 15 January 2007. We subset the data into clear-sky, cloudy and rainy scenarios using the CloudSat cloud classification product as well as the rain rate estimate. Figures 4 and 5 display clear-sky, cloudy and rainy simulated relationships between differential radar surface returns and surface pressure. As shown, there are good linear relationships between the differential radar returns and surface pressure even under moderate rain conditions. The rms_e in surface pressure varies from 3.6 to 6 hPa using scenario by scenario linear regressions. For example, an rms_e of 4.4 hPa was found by a linear regression using all the Stratocumulus simulations. Under clear-sky conditions, the spread found in these simulations is due to the different background conditions, in particular, temperature as demonstrated in Fig. 3. For cloudy and rainy conditions, the spread results from a mixture of different background conditions plus different hydrometeors. The hydrometeor influence is most evident in the moderate rain subplot.

The results shown in Figs. 4 and 5 are encouraging. They demonstrate that even with no ancillary knowledge of the atmospheric temperature or cloud scenario, surface pressure can be constrained to within a few hPa. Of course, such naive assumption is not expected as operational weather analysis can provide reasonable constraints on the atmospheric temperature and a range gated radar system would itself provide information on the cloud/precipitation scenario. Note that, subsetting the data using this ancillary knowledge will reduce the rms_e.

5 Error characterization and tone selection

To further study the capabilities of this technique, end-to-end retrievals were performed using one day of CloudSat-driven simulations as synthetic measurements. The retrieval

Full Screen / Esc

Printer-friendly Version

Interactive Discussion

algorithm used was a least squares fit following Rodgers (2000) and assuming hydrostatic equilibrium. These retrievals allow us to quantify both the precision and accuracy of the surface pressure retrievals when using ancillary knowledge of the atmospheric temperature or cloud/precipitation scenarios. The precision reflects the contribution from the measurement noise. The accuracy reflects systematic error sources, such as, the error due to the assumed temperature profile, the error due to the characterization of particulate extinction ($\sigma_{\text{Pext}}(\lambda, s)$) or the error due to the characterization in the surface backscatter ($\sigma^0(\lambda)$) properties.

The accuracy errors were estimated by an end-to-end retrieval exercise. Starting with a set of conditions regarded as truth we computed synthetic radar returns that were used as measurements and run through the retrieval algorithm. The retrieved surface pressure is regarded as a base for the comparisons. This set of conditions includes the pressure, temperature, gas concentration and hydrometeor vertical profiles, as well as perfect knowledge of the hydrometeor PSDs and surface backscatter (all these assumptions are described in Sect. 3). Then, for each systematic error a perturbed set of synthetic measurements were generated and ran through the retrieval algorithm. For instance, when computing the systematic uncertainty related to temperature, only the temperature values were perturbed, while the rest (IWC, LWC, rain, snow, PSDs, etc) were left unperturbed. The surface pressure retrieved for each of these perturbations is then compare to the base case. Table 1 summarizes the perturbations used.

Figure 6 shows the result of the uncertainty characterization for surface pressure retrievals under five different scenarios using 52.8 and 54.9 GHz radar tones. Using these particular tones with 0.05 dBZ instrument noise the precision estimate was 1.5 hPa. In general, for all sky conditions the most persistent potential error source was the assumed temperature profile; this uncertainty results in biases of no more than ~ 0.5 hPa. In cloudy but non precipitating situations this is followed by uncertainties due to errors in IWC and LWC as well as their corresponding PSD. For precipitating cases, the dominant source of uncertainty originates from errors in the rain and snow estimates as well as their corresponding PSD uncertainties; this can lead to worst case biases as

large as ~ 6.6 hPa. Lastly, uncertainties induced by possible errors in water vapor, and surface wind (which change the surface backscattering) are negligible.

End-to-end retrievals allows us to select the radar tones which minimizes the total error (precision plus accuracy). The precision can be thought as a measure of the signal to noise ratio of the measurement system. As already shown (see Fig. 1 – top), atmospheric attenuation varies drastically near the 60 GHz O_2 band; the closer to the band center, the stronger the O_2 absorption. Clearly, positioning both radar tones near the absorption wings will provide no surface pressure information because the absorption for the two radar tones will be almost equal. Tones close to the band center will provide no information because they are fully attenuated. Hence, frequencies with moderate O_2 absorption carry the most potential surface pressure information. Furthermore, these moderately O_2 absorbed frequencies should be spaced as far apart as possible to increase their spectral contrast, which translates to a better differential signal and therefore improves the precision of the retrieved surface pressure.

As a demonstration of the tone selection process, we highlight the nimbostratus case shown in Fig. 6. Figure 7 shows the precision and potential biases using all the possible combinations between 50 and 55 GHz every 0.5 GHz. As expected, precision increases with tone spectral separation, specifically 50 and 50.5 has the worst precision while 50 and 55 have the highest precision.

Also shown in Fig. 7 are the potential biases due to temperature, water vapor and hydrometeors. In principle, these biases should increase with tone separation because the spectral differences in the target optical properties increases (see Fig. 1). However Fig. 7 demonstrates that the increase in signal with tone separation dominates the potential increase in these biases. In general, this results in a decrease in retrieval biases with tone separation. Nonetheless, we note that the smallest hydrometeor and H_2O potential biases are found using 54 and 55 GHz, the two closest radar tones still containing pressure information.

In general, this suggests that the best pair of radar tones will depend upon the magnitude of the potential biases: (1) if they are considerably smaller than the precision the

best combination will be 50 and 55 GHz, (2) if they are significantly greater than the precision the best pair of tones will be 54 and 55 GHz, and (3) if they are comparable to the precision, the best pair will be such that both of them are as similar as possible.

To quantify this general conclusion for specific types scenarios we repeated this tone selection process for clear-sky, cloudy and precipitating conditions, constructed from CloudSat representative profiles spread through 2007. For each scene type, around 30 cases were selected. As expected, for non-precipitiating cases, the best combination was 50 and 55 GHz because the hydrometeor potential biases were small. For drizzle, the best combination was 53.5 and 55 GHz, because the hydrometeor potential biases had comparable levels to the precision. Lastly, for slight and moderate rain, where the error budget was dominated by the hydrometeor potential biases, we found that the best combination was 54 and 55 GHz.

The effects of using the optimum tone selection are shown in Fig. 8 which summarizes the result of the uncertainties characterization under the same scenarios shown in Fig. 6. Overall, the estimates of precision and the maximum potential biases decreased: for cloudy cases, precision improved to ~ 1.1 hPa (~ 0.4 hPa better than in Fig. 6) and for slight rain, the maximum potential biases due to hydrometeors decreased to ~ 4.5 hPa (~ 2 hPa less than before). Note that these radar tones are optimum in the sense that they should minimize the errors in a general sense, however there may be pairs of radar tones better suited for individual cases.

To test this technique under a wide range of conditions end-to-end retrieval simulations were performed for all the available CloudSat measurements from 15 January 2007 using the optimum tones. Under clear sky and cloudy conditions the precision of all the retrievals was improved to ~ 1.1, under drizzle rain it was ~ 1.6, and under slight and moderate rainy conditions it was ~ 2.1 hPa. Figures 9 and 10 show clear-sky, cloudy and precipitating maximum potential biases histograms. The potential biases 90 % of the time for clear sky and cloudy conditions will be less than ~ 1.1, for drizzle and slight rainy conditions will be less than ~ 2.4, and for moderate rain will be less than 3.4 hPa. Table 2 also lists the precision and potential maximum bias

for each scene type. Note that, due to the differential nature of this technique, even-though all the simulations were performed using a ocean backscatter model, these results are expected to be similar over land because the land surface backscattering coefficients ($\sigma^0(\lambda)$) is also weakly dependent on wavelength within the region of in-

5 terest. These results demonstrate that this technique holds considerable potential as a method for retrieving surface pressure under realistic clear sky through moderate precipitating scenarios.

6   Summary and conclusions

We have discussed the theoretical capabilities of a differential absorption radar tech-

10 nique to retrieved surface pressure under clear sky, cloudy and precipitating conditions. It was established that the differential radar returns near to the 60 GHz O_2 absorption region mostly depends upon surface pressure and temperature distribution. From this, it follows that assuming a temperature distribution it should be possible to invert a set of radar tones to retrieved surface pressure.

15 An inversion scheme was implemented focusing on the retrieval propagation of sys-tematic biases as well as random errors (the retrieval precision). This provided a tool to weight the surface pressure signal against errors introduced by uncertainties in other parameters needed by the retrieval such as the assumed temperature distribution, hy-drometeor abundances and particle size distributions.

20 To find optimum radar tones for different scenarios (Cirrus, Altostratus, Altocumu-lus, Stratus, Stratocumulus, Cumulus and Nimbostratus, as well as, drizzle, slight and moderate rain), an ensemble of around 30 cases for each scenario was constructed using CloudSat data. Then, end-to-end retrievals were performed using all possible pairs of radar tones between 50 and 55 every 0.5 GHz. Ultimately, the best pair of

25 radar tones depends upon the magnitude of the potential biases. For biases smaller than the precision uncertainty the best pair is 50 and 55 GHz which increases the spec-tral contrast hence reducing the precision error. This is typically the case for clear-sky

Title Page

Abstract | Introduction

Conclusions | References

Tables | Figures

◄◄ | ►►

◄ | ►

Back | Close

Full Screen / Esc

Printer-friendly Version

Interactive Discussion

and cloudy scenarios. For biases greater than the precision uncertainty the best pair is 54 and 55 GHz which reduces the impact of the variation in particulate extinction with frequency. This is typical for slight and moderate rain scenarios. Lastly, for biases comparable to the precision, the best pair is such that both the precision and the biases are minimized.

Finally, using these optimum sets of radar tones, we inverted a whole day of Cloud-Sat measurements to show the capabilities of this technique under a wide range of conditions. Our results suggest a minimal radar system with tones at 50 and 55 GHz to maximize precision in the prevalent non-precipitating scenarios. Addition of a third tone at 54 GHz would provide an optimum platform for retrievals with precision betqter than 2 hPa in all sky conditions and commonly ∼ 1 hPa. Generally, worst case scenario biases will be less than 2 hPa, typically 0.5 hPa and 1 hPa for non-precipitating and precipitating conditions. These results demonstrate that this technique holds considerable potential as a method for retrieving surface pressure under realistic clear sky through moderate precipitating scenarios.

Future research will investigate the feasibility of using not only the surface returns but the atmospheric returns due to the hydrometeors in a given scene to invert vertical pressure profiles. This may allow us to derive the atmospheric scale height and thus the temperature profile in the lower troposphere.

References

Abel, S. J. and Boutle, I. A.: An improved representation of the raindrop size distribution for single-moment microphysics schemes, Q. J. Roy. Meteorol. Soc., 138, 2151–2162, 2012. 5802

5   Austin, R. T., Heymsfield, A. J., and Stephens, G. L.: Retrieval of ice cloud microphysical parameters using the CloudSat millimeter-wave radar and temperature, J. Geophys. Res., 114, D00A23, doi:10.1029/2008JD010049, 2009. 5804

Barton, I. J. and Le Marshall, J. F.: Differential-absorption lidar measurements in the oxygen A band using a ruby lidar and stimulated Raman scattering, Opt. Lett., 4, 78–80, 1979. 5797

10 Barton, I. J. and Scott, J. C.: Remote measurement of surface pressure using absorption in the oxygen A-band, Appl. Optics, 25, 3502–3507, 1986. 5797

Battaglia, A., Tanelli, S. Kobayashi, S., Zrnic, D., Hogan, R. J., and Simmer, C.: Multiple-scattering in radar systems: a review, J. Quant. Spectrosc. Ra., 111, 917–947, 2010. 5803

Bouniol, D., Protat, A., Plana-Fattori, A., Giraud, M., Vinson, J.-P., and Grand, N.: Comparison of airborne and spaceborne 95-ghz radar reflectivities and evaluation of multiple scattering effects in spaceborne measurements, J. Atmos. Ocean. Tech., 25, 1983–1995 doi:10.1175/2008JTECHA1011.1, 2008. 5803

Brown, G.: Quasi-specular scattering from the air–sea interface, in: Surface Waves and Fluxes, edited by: Plant, W. and Geernart, G., 2, Kluwer Academic, 1–40, 1990. 5800, 5803

20 Buehler, S. A., Eriksson, P., Kuhn, T., von Engeln, A., and Verdes, C.: ARTS, the atmospheric radiative transfer simulator, J. Quant. Spectrosc. Ra., 91, 65–93, 2005. 5802

Donovan, D. and Lammeren, A.: First ice cloud effective particle size parameterization based on combined Lidar and radar data, Geophys. Res. Lett., 29, 1006, doi:10.1029/2001GL013731, 2002. 5816

25 Eriksson, P., Ekström, M., Rydberg, B., and Murtagh, D. P.: First Odin sub-mm retrievals in the tropical upper troposphere: ice cloud properties, Atmos. Chem. Phys., 7, 471–483, doi:10.5194/acp-7-471-2007, 2007. 5801

Fitzgerald, J. W. and Spyers-Duran, P. A.: Changes in cloud nucleus concentration and cloud droplet size distribution associated with pollution from St. Louis, J. Appl. Meteorol., 12, 511–

30 516, 1973. 5801

Flower, D. A. and Peckham, G. E.: A Microwave Pressure Sounder, JPL Publication 78-68, Caltech, 1978. 5797

Gerber, H.: Microphysics of marine stratocumulus clouds with two drizzle modes, J. Atmos. Sci., 53, 1649–1662, 1996. 5801

Gunn, K. L. S. and Marshall, J. S.: The distribution with size of aggregate snowflakes, J. Meteorol., 15, 452–461, 1958. 5816

Hannel, R. A.: Determination of cloud altitude from a satellite, J. Geophys. Res., 66, p. 1300, 1961. 5797

Heymsfield, A., Bansemer, A., Field, P. R., Durden, S. L., Stith, J. L., Dye, J. E., Hall, W., and Grainger, C. A.: Observations and parameterizations of particle size distributions in deep tropical cirrus and stratiform precipitating clouds: results from in situ observations in TRMM field campaigns, J. Atmos. Sci., 59, 3457–3491, 2002. 5816

Hogan, R. J.: Multiscatter: a fast, approximate multiple scattering algorithm, University of Reading, available at; http://www.met.reading.ac.uk/clouds/multiscatter/ (last access: March 2013), 2013. 5802

Hogan, R. J. and Battaglia, A.: Fast lidar and radar multiple-scattering models. Part II: Wide-angle scattering using the time-dependent two-stream approximation, J. Atmos. Sci., 65, 3636–3651, doi:10.1175/2008JAS2643.1, 2008. 5800, 5803

Howell, W.: The growth of cloud drops in uniformly cooled air, J. Meteorol., 6, 134–149, 1949. 5801

Huber, D. L. and Vleck, J. H. V.: The role of Boltzmann factors in line shape, Rev. Mod. Phys., 38, 187–204, 1966. 5802

Hufford, G. A.: A model for the complex permittivity of ice at frequencies below 1 THz, Int. J. Infrared Milli., 12, 677–682, 1991. 5800

King, M. D., Radke, L. D., and Hobbs, P. V.: Optical properties of marine stratocumulus clouds modified by ships, J. Geophys. Res., 98, 2729–2739, 1993. 5801

Klein, L. A. and Swift, C. T.: An improved model for the dielectric constant of sea water at microwave frequencies, IEEE T. Antenn. Propag., 25, 104–111, 1977. 5803

Korb, C. L. and Weng, C. Y.: A theoretical study of a two-wavelength lidar technique for the measurement of atmospheric temperature profiles, J. Appl. Meteorol., 21, 1346–1355, 1982. 5797

Lawrence, R. Lin, B., Harrah, S., Hu, Y., Hunt, P., and Lipp, C.: Initial flight test results of differential absorption barometric radar for remote sensing of sea surface air pressure, J. Quant. Spectrosc. Ra., 12, 247–253, 2011. 5797

DiAR surface pressure retrievals

L. Millán et al.

Title Page

Abstract | Introduction

Conclusions | References

Tables | Figures

◄◄ | ►►

◄ | ►

Back | Close

Full Screen / Esc

Printer-friendly Version

Interactive Discussion

Lebsock, M. and L'Ecuyer, T. S.: The retrieval of warm rain from CloudSat, J. Geophys. Res., 116, D20209, doi:10.1029/2011JD016076, 2011. 5804

Li, L., Heymsfield, G. H., Tian, L., and Racette, P. E.: Measurements of ocean surface backscattering using an airborne 94-GHz cloud radar – implication for calibration of airborne and spaceborne W-Band radars, J. Atmos. Ocean. Tech., 22, 1033–1045, doi:10.1175/JTECH1722.1, 2005. 5800, 5803

Liebe, H. J., Hufford, G. A., and Manabe, T.: A model for the complex permittivity of water at frequencies below 1 THz, Int. J. Infrared Milli., 12, 659–675, 1991. 5800

Lin, B. and Hu, Y.: Numerical simulations of radar surface air pressure measurements at O_2 bands, IEEE T. Geosci. Remote, 2, 324–328, 2005. 5797, 5804

Marchand, R., Mace, G. G., Ackerman, T., and Stephens, G.: Hydrometeor detection using CloudSat – an earth-orbiting 94-GHz cloud radar, J. Atmos. Ocean. Tech., 25, 519–533, 2008. 5804

Marshall, J. S. and Palmer, W. Mc K.: The distribution of raindrops with size, J. Meteorol., 5, 165–166, 1948. 5816

McFarquhar, G. M. and Heymsfield, A. J.: Parameterization of tropical cirrus ice crystal size distribution and implications for radiatiave transfer: results from CEPEX, J. Atmos. Sci., 54, 2187–2200, 1997. 5801

Millán L., Read, W., Kasai, Y., Lambert, A., Livesey, N., Mendrok, J., Sagawa, H., Sano, T., Shiotani, M., and Wu, D. L.: SMILES ice cloud products, J. Geophys. Res., 118, 6468–6477, 2013. 5801

Partain, P.: CloudSat ECMWF-AUX Auxiliary Data Process Description and Interface Control Document, Cooperative Institute for Research in the Atmosphere, Colorado State University, 2007. 5804

Pickett, H. M., Poynter, R. L., Cohen, E. A., Delitsky, M. L., Pearson, J. C., and Muller, H. S. P.: Submillimeter, millimeter, and microwave spectral line catalog, J. Quant. Spectrosc. Ra., 60, 883–890, 1998. 5802

Ray, P. S.: Broadband complex refractive indices of ice and water, Appl. Optics, 11, 1836–1844, 1972. 5800

Read, W. G., Shippony, Z., and Snyder, W. V.: EOS MLS Forward Model Algorithm Theoretical Basis Document, Jet Propulsion Lab., Pasadena, CA, JPL D-18130/CL#04-2238, 2004. 5802

Title Page

Abstract | Introduction

Conclusions | References

Tables | Figures

◄◄ | ►►

◄ | ►

Back | Close

Full Screen / Esc

Printer-friendly Version

Interactive Discussion

Read, W. G., Shippony, Z., Schwartz, M. J., Livesey, N. J., and Snyder, W. V.: The clear-sky unpolarized forward model for the EOS Microwave Limb Sounder (MLS), IEEE T. Geosci. Remote, 44, 1367–1379, doi:10.1109/TGRS.2006.873233, 2006. 5800, 5802

Rodgers, C.: Inverse Methods for Atmospheric Sounding: Theory and Practice, Series on Atmospheric, Oceanic and Planetary Physics, Vol. 2, World Scientific, Singapore, 2000. 5806

Rothman, L. S., Rinsland, C. P., Goldman, A.,Massie, S. T., Edwards, D. P., Flaud, J. M., Perrin, A., Camy-Peyret, C., Dana, V., Mandin, J. Y., Schroeder, J., McCann, A., Gamache, R. R., Wattson, R. B., Yoshino, K., Chance, K. V., Jucks, K. W., Brown, L. R., Nemtchinov, V., and Varinasi, P.: The HITRAN molecular spectroscopic database and HAWKS (HITRAN atmospheric workstation): 1996 edition, J. Quant. Spectrosc. Ra., 60, 665–710, doi:10.1016/S0022-4073(98)00078-8, 1998. 5802

Sassen, K. and Wang, Z.: Classifying clouds around the globe with the CloudSat radar: 1-year of results, Geophys. Res. Lett., 35, L04805, doi:10.1029/2007GL032591, 2008. 5804

Sekhon, R. S. and Sirvastava, R. C.: Snow size spectra and radar reflectivity, J. Atmos. Sci., 37, 299–307, 1970. 5802

Singer, S. F.: Measurement of atmospheric surface pressure with a satellite-borne laser, Appl. Optics, 5, 1125–1127, 1968. 5797

Smith, S. D., Colles, M. J., and Peckham, G.: The measurement of surface pressure from a satellite, Q. J. Roy. Meteorol. Soc., 98, 431–433, 1972. 5797

Squires, P.: The microstructure and colloidal stability of warm clouds, Tellus, 10, 256–261, doi:10.1111/j.2153-3490.1958.tb02011.x, 1958. 5801

Stephens, G. L., Vane, D. G., Boain, R. J., Mace, G. G., Sassen, K., Wang, Z., Illingworth, A. J., O'Connor, E. J., Rossow, W. B., Durden, S. L., Miller, S. D., Austin, R. T., Benedetti, A., Mitrescu, C., and the CloudSat Science Team: The CloudSat mission and the A-train a new dimension of space-based observations of clouds and precipitation, B. Am. Meteorol. Soc., 83, 1771–1790, 2002. 5803

Tanelli, S., Durden, S. L., Im, E., Pak, K. S., Reinke, D. G., Partain, P., Hyanes, J. M., and Marchand, R. T.: CloudSat's cloud profiling radar after two years in orbit: performance, calibration, and processing, IEEE Geosci. Remote S., 46, 3560–3573, 2008. 5803

Tsay, S.-C. and Jayaweera, K.: Physical characteristcs of Arctic status clouds, J. Clim. Appl. Meteorol., 23, 584–596, 1984. 5801

Valenzuela, G. R.: Theories for the interaction of electromagnetic and oceanic waves – a review, Bound.-Lay. Meteorol., 13, 61–85, 1978. 5800, 5803

DiAR surface pressure retrievals

L. Millán et al.

Title Page

Abstract	Introduction
Conclusions	References
Tables	Figures

◄◄ | ►►

◄ | ►

Back | Close

Full Screen / Esc

Printer-friendly Version

Interactive Discussion

Willis, P. T.: Functional fits to some observed drop size distributions and parameterization of rain, J. Atmos. Sci., 41, 1648–1661, 1984. 5816

Wu, D. L.: EOS MLS cloud ice measurements and cloud-sky radiative transfer model, IEEE Geosci. Remote. S., 44, 1156–1165, 2006. 5801

5 Wu, J.: Mean square slopes of the wind-disturbed water surface, their magnitude, directionality, and composition, Radio Sci., 25, 37–48, doi:10.1029/RS025i001p00037, 1990. 5803

Yamamoto, G. and Wark, D. Q.: Discussion of the letter by R. A. Hanel, "Determination of Cloud Altitude from a Satellite", J. Geophys. Res., 6, p. 3596, 1961. 5797

Yum, S. S. and Hudson, J. G.: Maritime/continental microphysical contrasts in stratus, Tellus B, 10 54, 61–73, 2001. 5801

Table 1. Systematic uncertainties perturbations[*].

Perturbation	Amount	Comments
Temperature	3 K	Calculated as the average of 10 randomly perturbed profiles
Water Vapor	10 %	Applied at all heights
IWC error	50 %	–
LWC error	50 %	–
Rain error	50 %	–
Snow error	50 %	–
IWC PSD1	–	Heymsfield et al. (2002)
IWC PSD2	–	Donovan and van Lammeren (2002)
LWC PSD1	–	Lognormal distribution with a 6 µm mean radius and a 1.5 spread.
Rain PSD1	–	Marshall and Palmer (1948)
Rain PSD2	–	Willis (1984)
Snow PSD1	–	Gunn and Marshall (1958)
Surface Wind	$12\,\mathrm{m\,s^{-1}}$	–

[*] for the "unperturbed" characteristics see Sect. 3.

Table 2. "Optimum" radar tones.

Scene type	Radar Tones [GHz]	Precision[a] [hPa]	Potential bias[a] 80 % of the time [hPa]	Potential bias[a] 90 % of the time [hPa]
Clear Sky	50.0, 55.0	1.1	0.45	0.45
Cirrus	50.0, 55.0	1.1	0.45	0.50
Altostratus	50.0, 55.0	1.1	0.50	0.70
Altocumulus	50.0, 55.0	1.1	0.50	0.70
Stratocumulus	50.0, 55.0	1.1	0.55	0.90
Cumulus	50.0, 55.0	1.1	0.70	1.10
Nimbostratus	50.0, 55.0	1.1	0.70	1.00
Drizzle[b]	53.5, 55.0	1.6	1.35	1.65
Slight Rain[b]	54.0, 55.0	2.1	1.80	2.35
Moderate Rain[b]	54.0, 55.0	2.1	2.75	3.35

[a] Estimates computed using end-to-end retrievals for each of the CloudSat measurements available in 15 January 2007 (Figs. 9 and 10).
[b] Drizzle, slight, and moderate rain correspond to rain rates lower than 0.1, between 0.1 and 1, and between 1 and 10 mm h^{-1}, respectively.
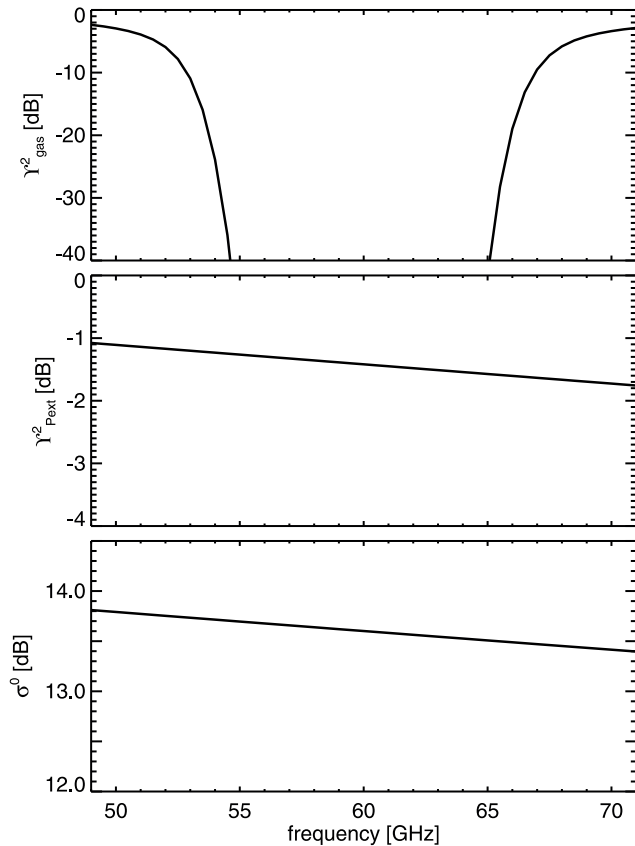
Figure 1. Typical atmospheric transmittance due to gases (top) and hydrometeors (middle) (Eq. 2) for a surface return journey (downward atmospheric pass, surface reflection, upward pass) for a nimbostratus cloud near the 60 GHz O_2 band region. (bottom) Ocean backscatter for a wind surface of $3\,m\,s^{-1}$ and temperature of $28\,°C$. Note that only the transmittance due to gases (top) show a significant frequency dependence.
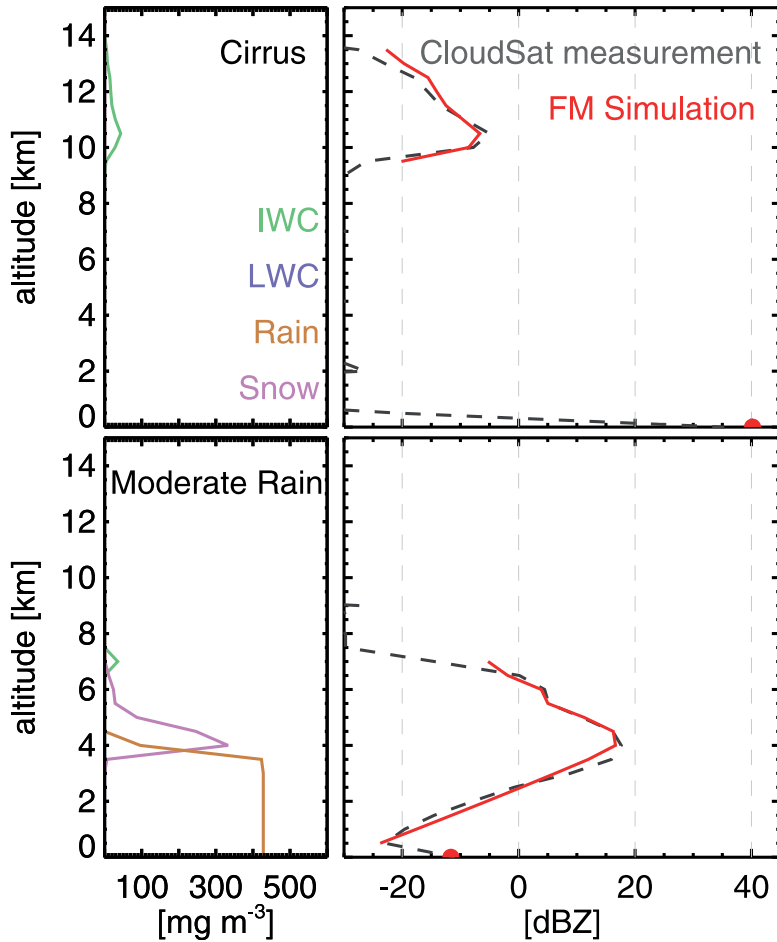
Figure 2. Comparisons between CloudSat measurements and forward model simulations. For a detailed description see Sect. 3.6.
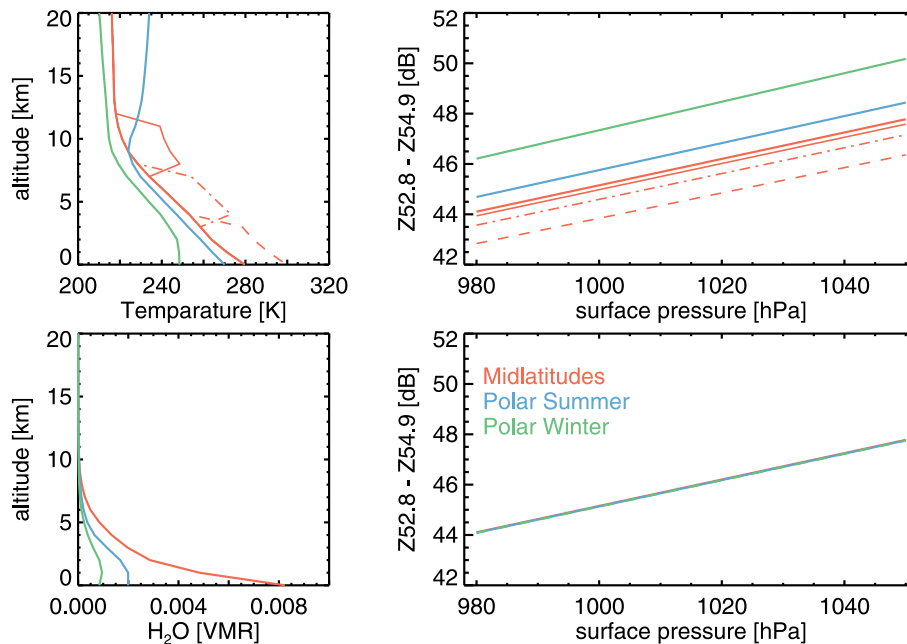
Figure 3. Simulated clear sky relationships between surface pressure and surface radar returns. The top row shows the effect of varying the temperature profile while the bottom shows the effect of varying water vapor. Each color coded point represents an adjustment of the entire pressure profile.
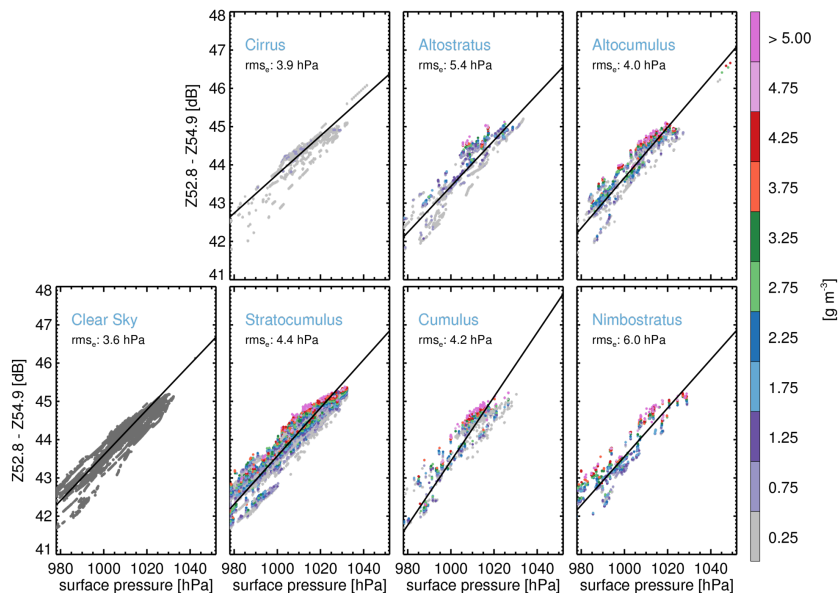
Figure 4. Simulated relationships between surface radar returns and surface pressure. Each point represents a CloudSat-driven simulation for each of the CloudSat measurements available in 15 January 2007 (Clear sky and cloudy cases only). The total hydrometeor column (for these cases IWC + LWC only) is color coded. Dark gray is used for clear sky cases (total hydrometeor column equal to zero). In each scenario, linear regressions for all cases as well as separated by total hydrometeors column are shown. The root mean square error (rms_e) displayed (black line) is the overall linear regression error when fitting all the cases for each scenario.

Printer-friendly Version

Interactive Discussion
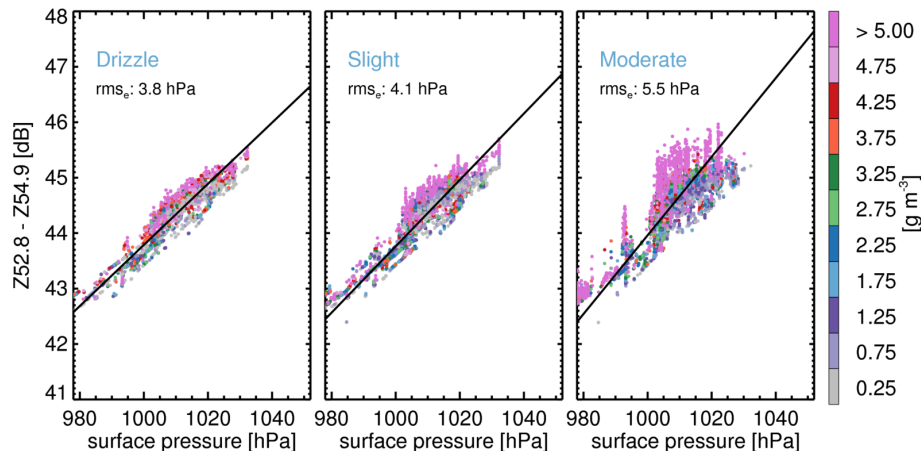
Figure 5. As in Fig. 4 but for precipitating cases. In this case, the total hydrometeor column includes IWC, LWC, rain, and snow. Drizzle, slight, and moderate correspond to rain rates lower than 0.1, between 0.1 and 1, and between 1 and 10 mm h^{-1}, respectively.

Full Screen / Esc
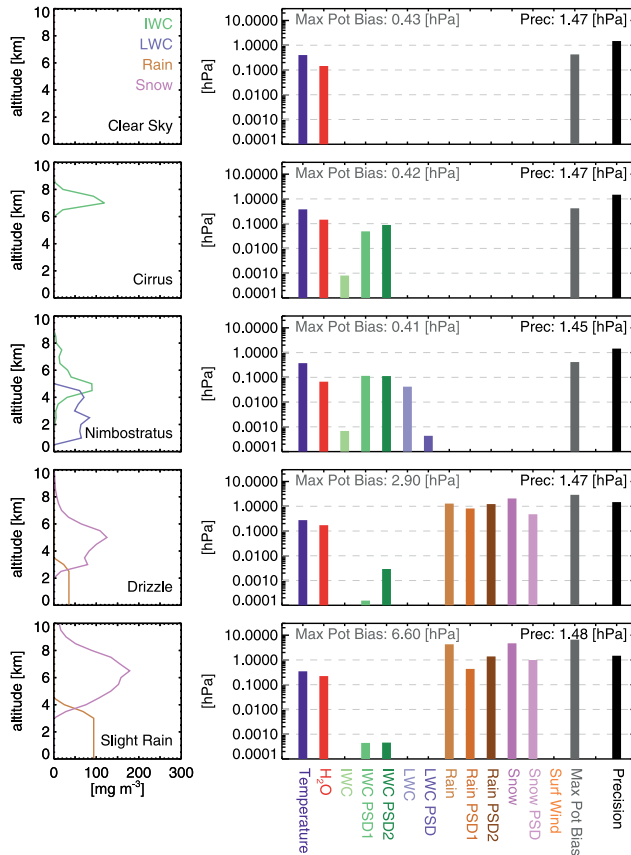
Figure 6. Systematic error estimates caused by each of the sources described in Table 1 as well as the precision and maximum potential bias for five different scenarios (Clear sky, Cirrus, Nimbostratus, drizzle and slight rain). The maximum potential bias is the root-sum-square combination of all the error sources shown. These simulations were performed using 52.8 and 54.8 GHz radar tones, simulation using optimum frequencies are shown in Fig. 8.
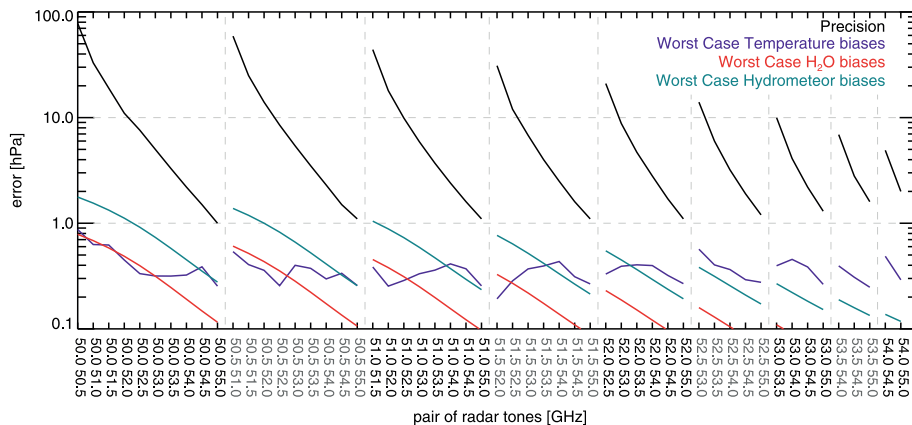
Figure 7. Precision and potential biases for the Nimbostratus case shown in Fig. 6 using all the possible combinations between 50 and 55 GHz every 0.5 GHz. The hydrometeor bias is the root mean square sum of the errors labeled IWC, IWC PSD1, IWC PSD2, LWC, LWC PSD, Rain, Rain PSD1, Rain PSD2, Snow, and Snow PSD in Fig. 6.
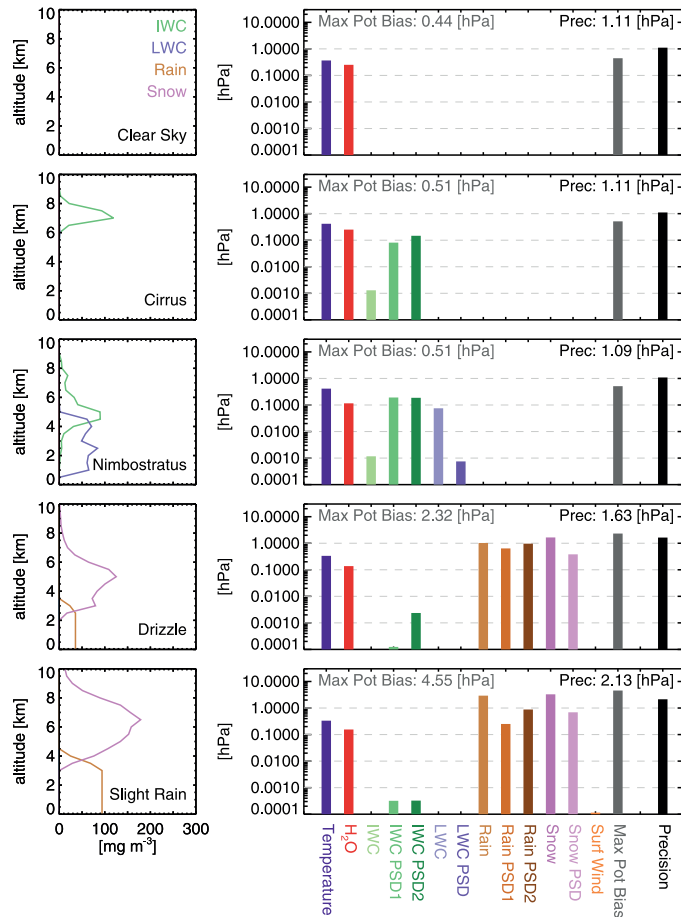
Figure 8. As Fig. 6 except these simulations were performed using the radar tones listed in Table 2.
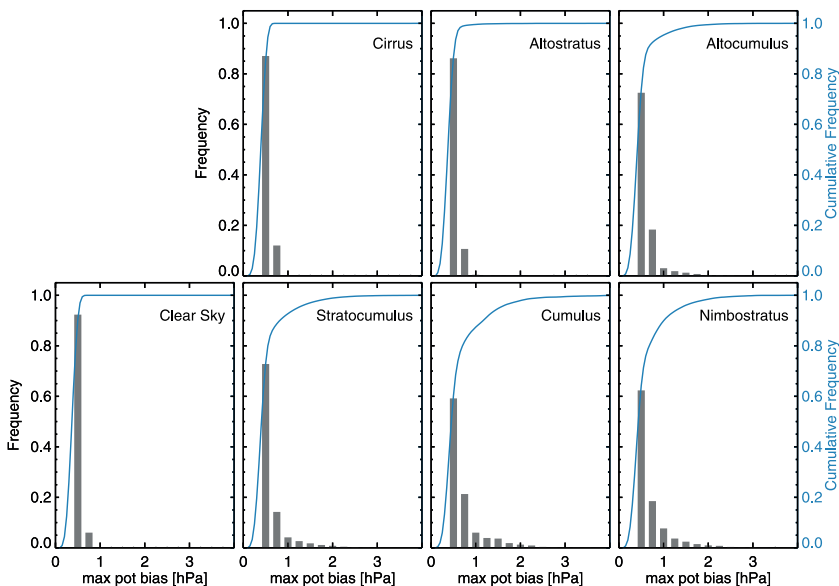
Figure 9. Histogram (gray) and cumulative histogram (blue) of the maximum potential biases for CloudSat-driven end-to-end retrievals for each of the CloudSat measurements available in 15 January 2007 (Clear sky and cloudy cases only).
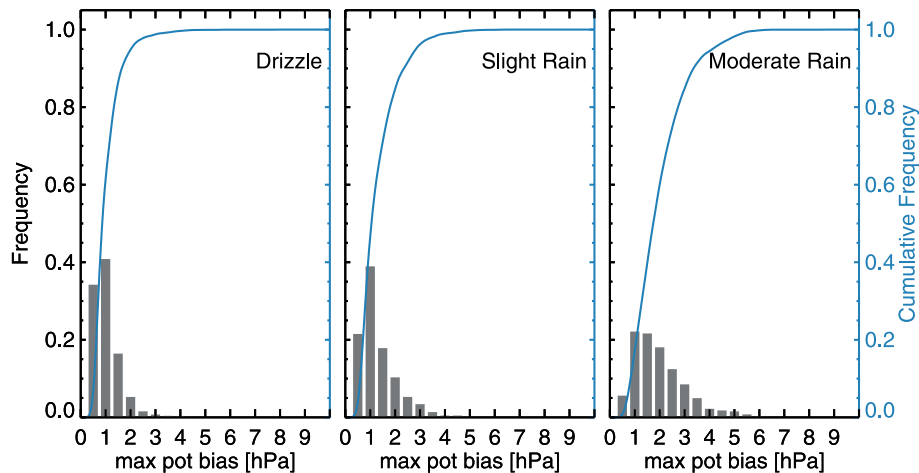
Figure 10. As in Fig. 9 but for precipitating cases.